

Defect reconstruction in a two-dimensional semi-analytical waveguide model via derivative-based optimization

J. Bulling, B. Jurgelucks, J. Prager, et al.

Citation: [The Journal of the Acoustical Society of America](#) **152**, 1217 (2022); doi: 10.1121/10.0013574

View online: <https://doi.org/10.1121/10.0013574>

View Table of Contents: <https://asa.scitation.org/toc/jas/152/2>

Published by the [Acoustical Society of America](#)





**Advance your science and career
as a member of the**

ACOUSTICAL SOCIETY OF AMERICA

LEARN MORE



Defect reconstruction in a two-dimensional semi-analytical waveguide model via derivative-based optimization

J. Bulling,^{1,a)}  B. Jurgelucks,²  J. Prager,¹ and A. Walther²

¹Bundesanstalt für Materialforschung und -prüfung, Unter den Eichen 87, 12205 Berlin, Germany

²Department of Mathematics, Humboldt-Universität zu Berlin, Unter den Linden 6, 10099 Berlin, Germany

ABSTRACT:

This paper considers an indirect measurement approach to reconstruct a defect in a two-dimensional waveguide model for a non-destructive ultrasonic inspection via derivative-based optimization. The propagation of the mechanical waves is simulated by the scaled boundary finite element method that builds on a semi-analytical approach. The simulated data are then fitted to given data associated with the reflected waves from a defect which is to be reconstructed. For this purpose, we apply an iteratively regularized Gauss-Newton method in combination with algorithmic differentiation to provide the required derivative information accurately and efficiently. We present numerical results for three kinds of defects, namely, a crack, delamination, and corrosion. The objective function and the properties of the reconstruction method are investigated. The examples show that the parameterization of the defect can be reconstructed efficiently as well as robustly in the presence of noise. © 2022 Author(s). All article content, except where otherwise noted, is licensed under a Creative Commons Attribution (CC BY) license (<http://creativecommons.org/licenses/by/4.0/>). <https://doi.org/10.1121/10.0013574>

(Received 6 April 2022; revised 29 July 2022; accepted 30 July 2022; published online 26 August 2022)

[Editor: Steffen Marburg]

Pages: 1217–1229

I. INTRODUCTION

Ultrasonic guided waves, especially Lamb-waves, are used in non-destructive testing (NDT) and structural health monitoring (SHM) to identify defects. Here, the long testing range that can be covered using guided waves is one of the main advantages over conventional scanning techniques. However, this advantage also yields new challenges. The multi-modal nature of guided waves with different wave velocities and the large distance between the defect and the sensor makes the localisation and characterisation of defects more difficult. On the other hand, Lamb-waves provide the flexibility to choose the most appropriate mode, which is the most sensitive to a specific type of defect.

Most models for crack identification assume that the data containing the waves scattered by the defect are available at certain sensor positions. Depending on the type of sensor, this data can be an electrical signal that represents a displacement or velocity field. We will refer to this data as measurement data, even though for many publications, including this one, it is generated artificially by appropriate simulations. There are two main types of methods to detect a defect in a waveguide. One approach is based on imaging to localise and characterise the defects. Another class of algorithms fits a damage model directly with the measured data. The resulting damage model can then be further analyzed, e.g., using fracture mechanics techniques. This also supports other objectives, such as NDT and SHM investigations, and can answer the question of whether the damage is severe and will lead to structural failure.

Most imaging algorithms assume a sensor network around the defect and consider a surface view of the waveguide as sketched in Fig. 1. Often these approaches are called guided wave tomography or migration in the seismic community. The measurement data are then propagated backwards from the sensors on the surface. As a possible method of backward propagation, each pixel of the surface is analyzed by the direct sound path between this pixel and the transmitter/receiver pairs.¹ This approach relies on the assumption that there is only one dominant wave mode to use its group velocity for the backward propagation. Other methods do not need a dominating mode, for example, if a time-reversal approach is utilized as backward propagation method.² There are many competing approaches for the backward propagation method. Since a full review is out of the scope of this introduction, we refer the reader to Refs. 3 and 4 for a comparison of the various methods. If the backward propagation method is defined by the transmitter/receiver-path, it depends strongly on the number of sensors and their position.³ In other cases, the resolution of these approaches is directly linked to the physical properties of the propagating waves, for example, the wavelength.² Most tomography algorithms show only a projection on the surface of the waveguide and do not show any depth of the defect.

As an alternative to the above imaging algorithms, the localization and characterization of defects can be viewed as an inverse problem, where one tries to find the set of parameters of a damage model that yield the smallest distance of the simulated data to the measurement data. These approaches consist of three main components. First, a forward model that generates simulated data representing the damage for the

^{a)}Electronic mail: Jannis.Bulling@Bam.de

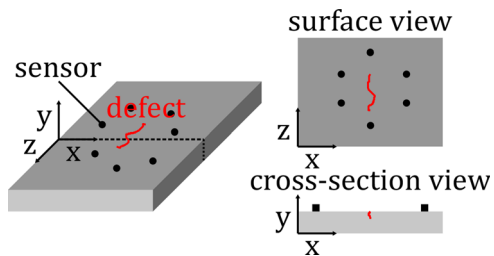


FIG. 1. (Color online) Different views for a 2D-simplification of the 3D-problem.

current set of parameters. Second, one uses an objective function that compares the measurement and simulation. Third, an optimization algorithm updates the parameter values to minimize the objective function, i.e., obtain a better fit of simulation and measurement. With regard to the simulation method, damage model, target function and optimization, there are different approaches that are briefly discussed in the following.

For a discrete damage model, the extended finite element method (XFEM) is often used, because of its possibility to define mesh independent cracks.⁵⁻⁹ Rabinovich *et al.*⁹ used the XFEM in the frequency domain to reconstruct a single straight crack. The objective function is based on the least square error between measurement and simulation data, oscillates and has several local minima. A genetic algorithm (GA) optimizes the objective function to overcome the difficulty of getting trapped in a local minimum. The same authors improved the results by switching to the time-domain⁹ and changing the objective function to one that is based on the “arrival time” of the reflection, which is often used in classic defect detection in an ultrasonic test. Using the arrival time, the objective function oscillates less, but there are still local minima. Livani *et al.*⁷ investigated multiple defects with particle swarm optimization. Finally, three dimensional problems with multiple cracks are solved by Agathos *et al.*⁵ They used a two-step GA approach for elliptical cracks. Jung and Taciroglu⁶ consider curved cracks and inclusions together with a gradient descent as the optimization method. Multiple optimization runs are performed with different starting points representing different cracks to circumvent local minima.

A time-reversal approach can also be used to optimize defect parameters. If a sensor signal is reversed in time and transmitted back in the domain, it will be refocused at the source. Amitt *et al.*¹⁰ defined an objective function based on refocusing the wave in a specific part of a membrane. The word membrane should indicate that the Helmholtz equation is solved instead of the elastic wave equation. Unfortunately, this objective function is oscillating.¹⁰ A full scan of the parameter space that defined the crack and its position was performed for optimization. An experimental validation of this approach is contained in Ref. 11.

Seidle and Rank¹² used another time-reversal approach for a membrane. An integral damage model is employed which lowers the stiffness for certain elements. The

connection between XFEM and a stiffness-reduction can be found in Ref. 13. This approach, also known as full wave-field inversion, allows many possible defect geometries and is not limiting their number, but the resolution of the defect depends on the computational grid. A highly refined computational grid can lead to very time-consuming calculations, especially for three-dimensional problems. A theoretical and experimental investigation of a similar approach can be found, e.g., in Rao and co-workers,¹⁴⁻¹⁶ where an acoustic inversion is used for elastic wave propagation to lower the computational demand. A change in both stiffness and density is considered in Ref. 16.

The approaches mentioned above exploit the surface of the waveguide, whereas also a cross section view may serve as alternative description, which is commonly utilized for waveguides. A plane strain simplification can be used to derive a two-dimensional problem—see Fig. 1. It is important to stress that these alternative dimensions of the cross-sectional view enable the analysis of the depth of the defect and the mode conversion due to defects with a certain depth. Wu *et al.*¹⁷ analyzed composite plates with the strip element method. The model allows investigating horizontal and vertical cracks in the cross section. Semi-analytical methods such as the strip element method have the advantage that the forward calculation is efficient. This simulation approach is combined with a genetic algorithm to perform the optimization.

Gravenkamp proposed another semi-analytical method, the scaled boundary finite element method (SBFEM), for simulating plate-like structures in the context of NDT and SHM.¹⁸ The SBFEM was first developed by Song and Wolf to compute bounded and unbounded domains with the same approach.^{19,20} The domain is divided into super elements. Quasi-polar coordinates, called scaled boundary coordinates, construct this first type of super element. For problems in the frequency domain, the super element has only degrees of freedom on the boundary, which leads to a reduction of one dimension in the computational cost. Later, Gravenkamp and co-workers used another coordinate transformation to construct super elements with a constant cross section for bounded and unbounded domains in two dimensions.^{21,22} These super elements are very efficient for simulating waveguides. The approach was extended to curved waveguides, three-dimensional waveguides, and waveguides with fluid/structure interaction.²³⁻²⁶ In addition to the simulation of unbounded domains, a discrete crack model is an essential development in SBFEM.²⁷ Quite recently, the SBFEM was used in a shape optimization scheme for a horn speaker and meta-materials²⁸ illustrating the flexibility of this formulation in the meshing process and with respect to infinite boundary conditions.

So far, the researcher examined only forward models with the SBFEM to investigate the wave-defect interactions for plate-like structures. In this contribution, we propose a general method for reconstructing a single discrete defect model inside a cross section model of a waveguide and solving the inverse problem. The SBFEM is used as an efficient forward model for the simulation with very few degrees of

freedom in the final linear system of equations. The defect reconstruction is formulated as an optimization problem and a derivative-based optimization algorithm is utilized to solve it in a systematic and efficient way. The technique of algorithmic differentiation (AD),^{29,30} provides the required gradient information exactly and with low computational costs. We analyse the resulting approach with respect to properties of the objective function, the reconstruction quality and the robustness against noise.

The remainder of this paper is organized as follows: The forward model and physical assumptions are presented in Sec. II. It is assumed that a particular defect type is present and that it is known which mode interacts most sensitively with that defect type at the chosen center frequency. Thus, the sensor arrangement and temporal excitation can be chosen accordingly. Section III summarizes the optimization scheme. This section includes several subsections. First, the objective function is discussed. This is followed by a summary of AD, on which gradient-based optimization is built. The third subsection describes the overall flow of the optimization. First, the approximate defect position must be determined; this serves as the initial value for the first defect parameter for the optimization. Then, in the next paragraph, the initial values of the remaining parameters are determined. The last paragraph finally presents the step-by-step optimization. In Sec. IV, three numerical examples are presented to show the versatility of the approach for different damage geometries. Conclusions are given in Sec. V. The Appendix contains additional implementation information.

II. SBFEM FORWARD MODEL

This section introduces the forward model to simulate the guided waves. Throughout, we consider only the two-dimensional case. As mentioned in the Introduction, the damage is incorporated directly into the waveguide model such that specific parameters define the damage. The forward model incorporates all important aspects of an ultrasound test on a waveguide. However, some aspects can only be designed for a specific experiment. Hence, certain simplifying assumptions have to be made to achieve greater general validity.

The first of these assumptions is that the defects are in a specific area within the waveguide modeled as an infinite domain. It is assumed that the vertical edges are far enough away from this area of interest so that the reflections from the vertical edges of the waveguide do not interfere with the reflections from the damage.

The second assumption is that the excitation by a sensor can be modeled by a traction force $\check{f}(\mathbf{x}, t)$ on one part of the boundary. This traction is mapped into the frequency domain by the Laplace-transformation. In contrast to the Fourier-transformation, the imaginary part of the Laplace-transformation should weaken the resonance and wrap-around effects of the numerical model. In the discrete-time

version, this procedure, known as the exponential window method (EWM),³¹ is given by

$$\check{f}(\mathbf{x}, t) = \mathbf{f}(\mathbf{x})\check{\tau}(t) = \mathbf{f}(\mathbf{x}) \sum_{n=0}^N (\tau_{\omega_n} \exp(-i\omega_n t) + \text{c.c.}), \quad (1)$$

where c.c. denotes the complex conjugated of the previous term. The complex angular frequency $\omega_n = (n\omega_\Delta - i\zeta) \in \mathbb{C}$ is defined by a uniform frequency step ω_Δ and a small parameter ζ . Note that only the real part of the complex angular frequencies changes.

Algorithmically, the EWM is implemented in the following three steps:

- (i) Multiply $\check{\tau}(t)$ with the window function $\exp(-\zeta t)$ with $\zeta = 0.5\omega_\Delta$, where the frequency step ω_Δ results from the time vector, use the fast-Fourier-transform (FFT) on the product, and search for the relevant frequencies.
- (ii) Approximate the displacement spectrum for all relevant complex frequencies ω_n [see Eqs. (3) and (4)].
- (iii) For evaluation in the time-domain, transform the displacement by the inverse FFT and afterwards multiply the inverse window function $\exp(\zeta t)$.

For all examples, the time dependent part $\check{\tau}(t)$ of the excitation is a sin-modulated Gaussian pulse, i.e.,

$$\check{\tau}(t) = \sin(2\pi f_c t) \exp\left(-\frac{(t-t_c)^2}{2f_c^{-2}}\right) \quad (2)$$

with the center frequency $f_c = 200$ kHz and a time shift of $t_c = 5f_c^{-1}$. Figure 2(a) shows the pulse in the time-domain, while Fig. 2(b) illustrates the spectrum. Additionally, the plot presents the dispersion curves of the group velocity associated with the waveguides in the numerical examples. The dispersion curves are computed with the SBFEM.²² This figure shows that the relevant spectrum of the excitation is in the range where only the two fundamental modes propagate.

For each discrete angular frequency step, the SBFEM is used to approximate the displacement in the equations of linear elastodynamics

$$\begin{aligned} \nabla \cdot \boldsymbol{\sigma}(\mathbf{u}(\mathbf{x})) + \omega_n^2 \rho \mathbf{u}(\mathbf{x}) &= \mathbf{0}, & \mathbf{x} \in \Omega \subset \mathbb{R}^2, \\ \boldsymbol{\sigma}(\mathbf{u}(\mathbf{x})) \mathbf{n} &= \mathbf{f}(\mathbf{x}) \tau_{\omega_n}, & \mathbf{x} \in \Gamma, \end{aligned} \quad (3)$$

with the displacement $\mathbf{u} = (u_x, u_y)^\top$, the linear stress tensor $\boldsymbol{\sigma}$, the density ρ , and where \mathbf{n} is the outer normal vector. The linear stress tensor $\boldsymbol{\sigma}$ is given by Hooke's law, $\boldsymbol{\sigma} = \mathbf{C} : \boldsymbol{\varepsilon}$, and the linear strain-displacement-relationship, $\boldsymbol{\varepsilon} = 0.5((\nabla \mathbf{u})^\top + (\nabla \mathbf{u}))$, where \mathbf{C} is the fourth-order elasticity tensor, that is defined by the material parameters, and $\boldsymbol{\varepsilon}$ is the strain.

As for many other numerical methods, when using the SBFEM, the PDE in Eq. (3) is converted into systems of linear equations

$$\mathbf{S}_{\omega_n} \mathbf{u}_{\omega_n} = \mathbf{f}_{\omega_n} \quad (4)$$

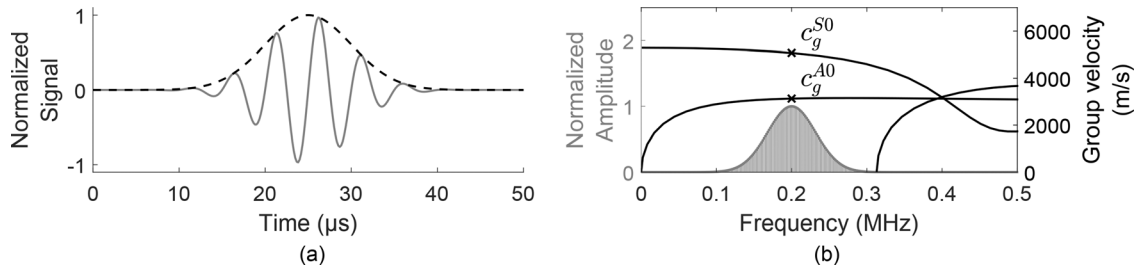


FIG. 2. Time and frequency dependency of the excitation signal in Eq. (2). (a) Excitation signal $\tilde{\tau}$ in the time-domain. (b) Excitation signal τ in the frequency-domain.

with the global, dynamic stiffness matrix \mathbf{S}_{ω_n} that depends on the complex angular frequency, the nodal displacement vector \mathbf{u}_{ω_n} , and the global traction vector \mathbf{f}_{ω_n} . To compute the global dynamic stiffness matrix \mathbf{S}_{ω_n} , the domain has to be sub-divided into super elements, i.e., $\Omega = \cup_{k=1}^K \Omega_k$. Figure 3 shows such a subdivision into super elements. For each super element Ω_k , parts of the boundary are meshed with 1D finite elements with two degrees of freedom per node—one degree for u_x and the other for u_y . Mainly, eigenvalue decompositions are used to compute the local stiffness matrix $\mathbf{S}_{\omega_n}^k$ for each super element Ω_k . These local stiffness matrices are then assembled into the global matrix, while the global traction vector is assembled directly from the 1D boundary finite elements. The 1D edge finite element approximation uses spectral shape functions based on the Gauss-Lobatto points. For example, Fig. 3 shows elements with shape functions of degree $p = 4$ with five nodes (marked with \bullet). The vertices of the finite elements may depend on a parameter set q_i , which is later modified by the optimization process. Only the vertices of the elements near the defect can be changed by the optimization algorithm, while the elements near the excitation are independent of the parameters.

The rectangular super elements are used to approximate the extended parts of the waveguide. Figure 3 shows examples with the super elements $\Omega_1, \Omega_3, \Omega_4$, and Ω_6 . These super elements require a constant cross section. The cross section parallel to the y axis is then meshed with the 1D finite elements and scaled in the x -direction. If the super element is finite, as Ω_3 in Fig. 3, the finite element meshes must coincide on both sides. Note that the length in x -direction does not influence the computational cost because there are only nodes at the cross-sections. The low number of nodes leads to a very efficient calculation for long parts of the domain. The outer boundaries parallel to the x -direction, illustrated by thin lines in Fig. 3, have

traction-free conditions. Rectangular super elements can also approximate semi-infinite parts of the model, see, e.g., Ω_1 and Ω_6 in Fig. 3. So, the models assume that there are no reflections at the ends of the plate. For the derivation of the local stiffness matrix of the super element, see Refs. 21, 32. The main part of the computation to set up the local stiffness matrix is an eigenvalue problem. A direct formula³³ computes the derivative of the eigenvalue problem inside the differentiated algorithm when applying AD.

The super element that forms a star-convex polygon is always required when the rectangular super element can no longer define the geometry or boundary conditions. Here, 1D a finite element line mesh is scaled toward a single point. The single point is called the scaling center. In the figures, the thin lines meet in the scaling center. In general, the position of the scaling center can be dependent on the parameter set q_i to be determined by the optimization, but this is only the case for super elements near the defect. The super element only needs nodes on the boundary yielding a high level of effectiveness. An additional special feature is that the super element also provides a simple crack model because a double node can introduce it. The crack is illustrated in Ω_5 (see Fig. 3), where a red node marks the double node. The red line is a traction-free boundary due to the double node. Despite the crack tip singularity, one still observes exponential convergence under p -refinement^{34–36} using such super elements. For the derivation of the local stiffness matrix of the super element, we followed Ref. 37. The derivation of the local stiffness matrix is quite involved. A continued-fraction-based approach builds on one algebraic Riccati equation and several algebraic Lyapunov equations.^{38,39} In this paper, both algebraic equations are solved by an eigenvalue decomposition within the SBFEM algorithm. The solution of the Riccati equation can be found in Ref. 39, while the Lyapunov equation is solved in the Appendix.

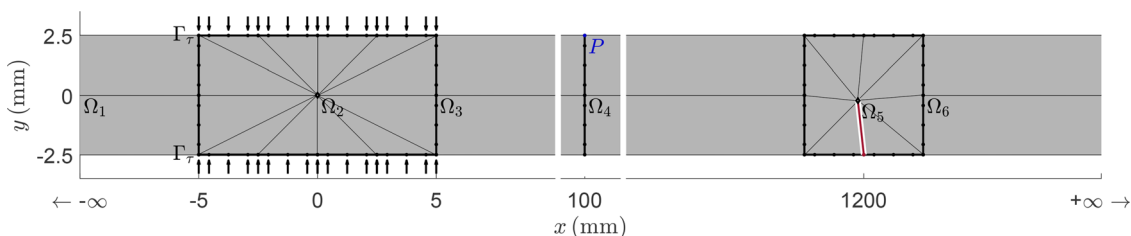


FIG. 3. (Color online) SBFEM model for the waveguide with a crack with degree $p = 4$. The \mathbf{q} -dependent defect is marked in red with a white border at $x = 1200$ mm.

It is worth mentioning that previous investigations have shown that polygonal super elements are quite robust for small and large finite element sizes inside the same mesh.⁴⁰ This robustness is important if geometric optimization changes the element sizes on the fly.

III. THE ADAPTED OPTIMIZATION APPROACH

A. The inverse problem

In general, the procedure described here to identify the defect properties is an indirect method. The aim is to solve the inverse problem

$$\min_{\mathbf{q} \in \mathcal{Q}} \|\mathbf{F}(\mathbf{q}) - \mathbf{y}_{meas}\|^2, \tag{5}$$

where \mathbf{y}_{meas} is given by physical measurements performed to detect the defect and $\mathbf{F}(\mathbf{q}) : \mathbf{q} \mapsto \mathbf{y}_{sim}$ denotes the *forward operator*. The forward operator is given by a simulation of the same quantity assuming that the defect is characterized by some vector \mathbf{q} . The forward operator is a short notation for the EWM together with the SBFEM-model described in Sec. II. The space \mathcal{Q} and its elements $\mathbf{q} \in \mathcal{Q}$ represent one possible parameterization of the considered defect. For the examples considered in this article the space \mathcal{Q} is scaled to $[1, 2]^N$, where $N = 2$ or $N = 3$ is the dimension of the parameter space. This scaling to the same range of values for all parameters supports the solution of the inverse problem. Solving the optimization problem (5), one obtains a parameterization \mathbf{q}^{min} for the defect which best approximates the measurement data.

In practice, inverse problems are usually hard to solve for several reasons. First, the resulting optimization problem need not (and generally does not) have a unique solution which may not depend continuously on the measurement data \mathbf{y}_{meas} . Such inverse problems are called *ill-posed* problems and are prevalent throughout almost all applications of parameter identification problems. In order to solve ill-posed problems, one is usually well-advised to deploy custom-tailored regularization techniques to the problem.

On the other hand, a different issue that may arise is that the error function in Eq. (5) may be hard to optimize as it may have adverse optimization properties such as not

being sufficiently smooth or incorporating many only locally optimal points. In this case, it may be advantageous to modify the forward operator \mathbf{F} and the measurements \mathbf{y}_{meas} so that the objective function is better suited for optimization purposes.

A simple approach uses the response data measured directly at a point. The y -component is more interesting as the x -component because of its practical relevance. For example, a single laser Doppler vibrometer measures the y -component of displacement or velocity, depending on the type of measurement method. We will assume that the displacement is measured, i.e.,

$$(\tilde{\mathbf{y}}_{meas})_i = u_y(t_j, P), \tag{6}$$

where u_y is the y -displacement and $t_j = (j - 1)\Delta t$, $j = 1, \dots, J$, are the discrete time steps. In this contribution, the time step is $\Delta t = 1/(30f_c) = 1/6 \mu s$ and the last index is $J = 15\,000$. Since the displacement and the velocity have very similar characteristics, all results are transferable to the velocity. For all numerical examples, the first geometric parameter is the global position of the defect. Figure 4(a) shows in gray the y -displacement of the model in Fig. 3 at the point P for the global defect x -position q_1 , where the other parameters, crack depth and angle, are kept constant at 1.5. Additionally, the envelope of the signal is shown in black or dark green. Figure 4(b) depicts the objective function based on the displacement, where the middle (green) signal in Fig. 4(a) is used as measurement data $\tilde{\mathbf{y}}_{meas} = \mathbf{F}(\mathbf{q}^*)$. However, as the waveguide is excited via a sinusoidal pulse, the measured displacement also incorporates the oscillating behavior. In fact, one can see that the objective function (5) also inherits these features, see Fig. 5(a) for illustration, which is a rotated detailed view of the dashed box in Fig. 4(b). We note that the resulting objective function has many only locally optimal points near the global optima. Hence, many optimization methods would have difficulties solving this optimization problem to global minimality.

The authors also experimented with different variations of the data such as using the spectrum of the response. However, the problem caused by many local minima remained. Many tests we conducted have shown that the measurement data

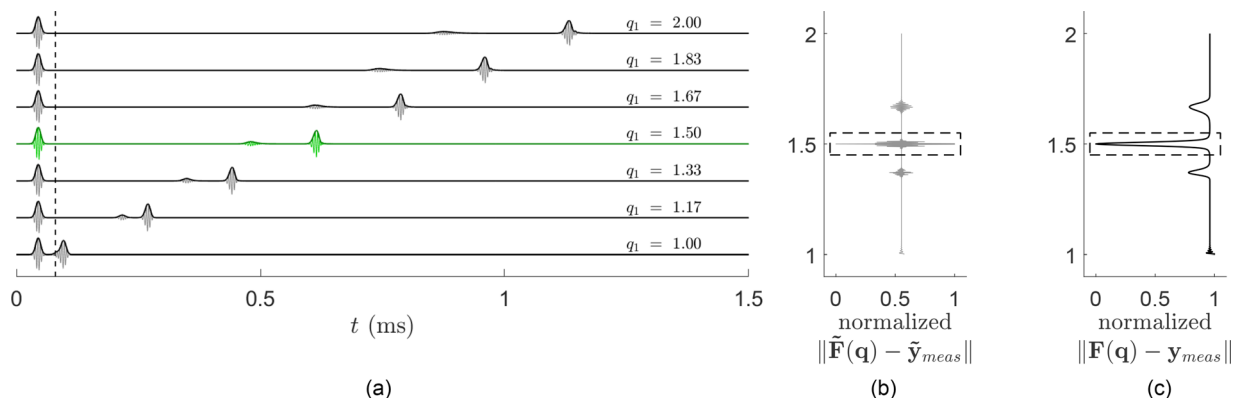


FIG. 4. (Color online) Signals and objective functions for the waveguide with a crack. (a) Response u_y and envelope e_y at point P . (b) u_y -based objective function $\tilde{\mathbf{F}}$. (c) e_y -based objective function \mathbf{F} .

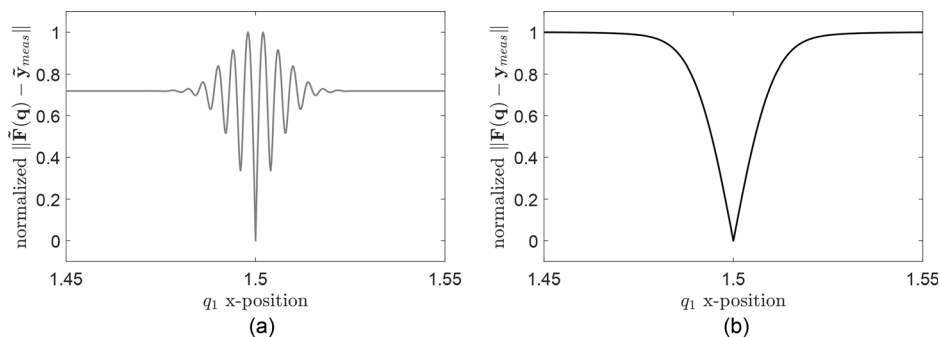


FIG. 5. Comparison of the different objective functions in a detailed view of the dashed box in Figs. 4(b) and 4(c), respectively. (a) Objective function $\tilde{\mathbf{F}}$ based on the y -displacement. (b) Objective function \mathbf{F} based on the envelope of the y -displacement.

with the best characteristics from the optimization point of view is the envelope of the displacement, i.e.,

$$(\mathbf{y}_{meas})_i = e_y(t_j, P) \quad \text{with} \quad e_y = \text{env}(u_y), \quad (7)$$

where env is the envelope function over time calculated via a Hilbert transformation. Analogous to the pure displacement, Fig. 4(c) shows the objective function for all crack positions between the middle (green) envelope in Fig. 4(b) with a forward operator \mathbf{F} which included the calculation of the envelope. Figure 5(b) shows the detailed view around the global minimum.

In addition to the global minimum, Fig. 4(c) shows two local minima. These local minima are associated with the mode conversion. The excitation, to the left of the dashed line, is a pulse that corresponds to the S0-mode. However, the S0-mode and the mode converted A0-mode are reflected. If the S0-wavepackage of the forward simulation is at the position of A0-wavepackage of the measurement data, this leads to a local minimum. Compare the middle (green) line with the line above in Fig. 4(a). Our approach to circumvent the local minima is to get a sufficient good initial guess, which lies near the global minimum. The details of the initial guess can be found below.

For the rest of the paper, the measurement data \mathbf{y}_{meas} is the envelope of the y -displacement at a single point P for all time steps [Eq. (7)], while the forward operator \mathbf{F} includes the calculation of the envelope. Please note that using the displacement data directly for optimization yields the same results as when using envelope data if the starting values were obtained by the optimization method described below based on only the envelope data. Hence, solely using the unmodified displacement data yields no benefit with regard to global solutions of the optimization problem.

B. Algorithmic differentiation

In order to use gradient-based optimization methods for the reconstruction of defects, derivatives of solutions of the partial differential equation are required. These could be approximated via finite differences (e.g., Ref. 6) or computed by setting up and solving the adjoint equation of the partial differential equation considered (e.g., Refs. 12 and 14) We tested the use of finite differences and found the approximation to be insufficient for the optimization procedure. Furthermore, in the development phase of this project we experimented with different boundary conditions. Hence, an

adaptation of the adjoint equation as a time-consuming and error-prone process would have been necessary in order to compute derivatives via the adjoint approach.

Therefore, we apply algorithmic differentiation (AD), also called automatic differentiation, which provides derivative information of arbitrary order for a given code segment. The derivatives are provably accurate up to working accuracy due to the fact that the computer program evaluating the function is broken down into a sequence of elementary evaluations upon which the chain rule of calculus is systematically applied. There are numerous AD tools available for a wide range of programming languages, see the website in Ref. 41 for an overview of tools and references. Since our forward operator described in detail in the previous section is implemented in MATLAB, we apply the AD-tool ADiMat⁴² to compute derivatives of solutions of the partial differential equations. Some mild modifications to the code were necessary such as computing derivatives of the Lyapunov equation which originally was not available in ADiMat.

C. The resulting optimization procedure

Even though we made some effort to reformulate the objective function (5) so that it is easier to optimize, we cannot eliminate all issues entirely. Hence, in this subsection, we present the optimization algorithms that we deployed.

A first simple approach for the solution of the optimization problem (5) is to use standard optimization software naively. This can involve derivative-based approaches such as IPOPT,⁴³ WORHP,⁴⁴ or the optimization routine `fmincon` provided by MATLAB. Alternatively, one may use derivative-free approaches such as coordinate descent, genetic optimization or other heuristic-based optimization methods like particle-swarm methods.

Derivative-based optimization algorithms have the great benefit of fast and provable convergence but generally only converge locally. With derivative-free methods often there is the hope associated that these methods converge globally. However, global convergence cannot be proven. Moreover, the whole optimization procedure may require thousands of function evaluations. The required number of evaluations is of particular significance as the simulation in our case involves solving a partial differential equation; thus, one objective function evaluation is already quite expensive—solving the partial differential equations many times is simply impractical.

In light of these facts, the approach presented here is a two-step approach: We first generate a refined initial guess for all variables. After a good initial point is established, we deploy a gradient-based optimization with fast convergence properties.

1. Initial guess for the global position

As mentioned above, the first geometric parameter q_1 is the global position of the defect for all numerical examples. To get an initial guess for the defect position q_1 , we consider the time of flight to get a physical position L_1 inside the waveguide. This physical position is then mapped linearly into the parameter space. The physical position of the defect L_1 can be estimated by

$$L_1 \approx T_\Delta \frac{c_g^{ex} \cdot c_g^{re}}{c_g^{ex} + c_g^{re}}, \tag{8}$$

where T_Δ is the time of flight, c_g^{ex} is the group velocity at the center frequency of the excited mode, and c_g^{re} is the group velocity of the reflected mode with the highest amplitude. For all our examples prior investigations have shown that the highest reflections for the y -component are always associated with the A0-mode [see Fig. 4(a)], so the reflection velocity c_g^{re} is the A0-group velocity c_g^{A0} at the center frequency—see Fig. 2(b).

The computation of the time of flight T_Δ is based on cross-correlating the excitation pulse with the rest of the signal. The excitation pulse is separated by a defined threshold T_{ex} from the reflections. If the envelope of the cross correlation is maximal, the argument is an approximation of the time of flight, i.e.,

$$r(t) = \text{env}(u_y(t, P)[t < T_{ex}] \star u_y(t, P)[T_{ex} \leq t]), \tag{9}$$

$$T_\Delta = \text{argmax}_t r(t), \tag{10}$$

where \star is the cross correlation operator and $[\cdot]$ is the Iverson bracket. The Iverson bracket is one if the statement inside is true and zero otherwise. Figure 4(a) shows the threshold as a dashed line, and the excitation pulse is on the left side while the rest of the signal is on the right side. In the presented examples, the function $r(t)$ has a distinct maximum, which is associated with the A0-mode. However, if there is any ambiguity in the maximum value or the mode associated with the maximum value, it is a straightforward option to run the inverse method with multiple start values for the first parameter.

2. Refined initial guess for all parameters

In order to obtain a refined initial guess for the gradient-based optimization, we can use Eq. (8). The approximation for the first coordinate given there is fairly accurate and is located within the valley of the objective function, see Fig. 5(b). However, with a simple line-search in the vicinity of the valley, the accuracy of the initial guess can be greatly improved. This simple line-search requires very few function evaluations, and the computational cost is insignificant. The accuracy of the first coordinate is important as inaccurate values lead to locally optimal values (especially in the presence of noise) for the other coordinates with which optimization methods have difficulty escaping. The other coordinates are determined by selecting the

vector with the smallest objective function from M random vectors, where our default value of M is 10. As the line-search is computationally very cheap, we also refine the other coordinates in the same fashion, beginning with the least critical or problematic coordinates. Due to many only locally optimal points, see Fig. 11(a), the amount of randomly selected points is increased to 100 for corrosion-type defects. The whole procedure is sketched in Algorithm 1.

ALGORITHM 1: Refined initial guess

-
-
- 1: Evaluate Eq. (8) for an initial guess of the first coordinate.
 - 2: Sample M random points $\mathbf{q}_0^1, \dots, \mathbf{q}_0^M \in \mathcal{Q}$ for the remaining second and possibly third coordinate.
 - 3: Evaluate corresponding objective values $\|\mathbf{F}(\mathbf{q}_0^m) - \mathbf{y}_{meas}\|^2, m = 1, \dots, M$ and select \mathbf{q}_0^m with the smallest objective value.
 - 4: Apply coordinate-wise line-search to \mathbf{q}_0^m to decrease the objective function value. The resulting parameter is \mathbf{q}_0 .
-
-

3. The stepwise optimization procedure

One way to deal with an objective function that has many locally optimal points is to introduce regularizing techniques. Hence, instead of solving the original problem (5) we add a Thikonov-type regularization term

$$\min_{\mathbf{q} \in \mathcal{Q}} \|\mathbf{F}(\mathbf{q}) - \mathbf{y}_{meas}\|^2 + \alpha_k \|\mathbf{q} - \mathbf{q}_0\|^2. \tag{11}$$

This new problem has much better theoretical and practical properties. If the regularization parameter α_k is large, the optimization problem is dominated by the second term which is a convex problem with a unique solution. However, as we are interested in solving the original problem we choose a monotonically decreasing sequence $\alpha_k \rightarrow 0$ for an iterative procedure $k \rightarrow \infty$. For $\alpha_k \approx 0$ we get a solution to the original problem. By further linearizing the first term a unique solution for each step is given by the so called iteratively regularized Gauss-Newton method (IRGNM), see, e.g., Ref. 45.

The overall procedure is given in Algorithm 2, where \mathbf{F}' is the Jacobian matrix of the forward operator, \mathbf{I} is the identity matrix, and $(\cdot)^H$ denotes the adjoint operator. In this work, the regularisation parameter is updated by $\alpha_{n+1} = 0.9 \cdot \alpha_n$.

ALGORITHM 2: Iteratively regularized Gauss-Newton method (IRGNM)

-
-
- 1: Initialize \mathbf{q}_0 and $(\alpha_n)_{n \in \mathbb{N}} \rightarrow 0$
 - 2: **for** $n = 0, \dots, \text{maxiter}$ **do**
 - 3: $\mathbf{q}_{n+1} = \mathbf{q}_n + (\mathbf{F}'(\mathbf{q}_n)^H \mathbf{F}'(\mathbf{q}_n) + \alpha_n \mathbf{I})^{-1} (\mathbf{F}'(\mathbf{q}_n)^H (\mathbf{y}_{meas} - \mathbf{F}(\mathbf{q}_n)) + \alpha_n (\mathbf{q}_0 - \mathbf{q}_n))$
 - 4: **if** $\|\mathbf{q}_{n+1} - \mathbf{q}_n\| < \epsilon$, **then**
 - 5: $\mathbf{q}^{\min} = \mathbf{q}_{n+1}$
 - 6: **STOP**
-
-

IV. NUMERICAL EXPERIMENTS

In this section, we present several numerical examples to show the versatility of the approach. Each model considers a

different type of defect. The first example is about classic crack identification. The second example shows a similar set-up but tries to find a horizontal crack or rather a delamination defect. The third type of defect is a model of a corrosion defect.

All waveguides in the following examples are made out of steel. The isotropic material parameters are given in Table I, and for all waveguides a plane strain is assumed. All meshes use shape functions of degree $p = 4$, i.e., elements with five nodes. The necessary degree is determined in advance by investigating the critical geometric parameter. For example, the smallest and the largest crack length are the critical geometric parameter for the first model. For all our models, a simulation with a degree of $p = 4$ leads to a difference in the signals below 0.1% compared to a simulation with $p = 5$. It is worth noting that there are numerous convergence studies for the SBFEM^{34,36,37,46} and the code is thoroughly validated using commercial FEM tools.

A. Waveguide with a crack

This example considers a steel plate with a single straight crack. Figure 3 shows an overview of the model. Note that the x axis is interrupted to fit the model into the figure. The left side of Fig. 3 depicts the excitation of the plate. Arrows in Fig. 3 show the area and direction where spatially constant traction is applied. Note that the phase angle of the excitation is contained by the phase of the complex value τ_{ω_n} in Eq. (3). At these parts, the excitation takes place by a normal traction force

$$f_{S0}(\mathbf{x}) = -\mathbf{n} [\mathbf{x} \in \Gamma_\tau]. \tag{12}$$

The traction is a model for the excitation of a double transducer set-up⁴⁷ that can produce both fundamental modes by applying a force in the same or opposite direction on the plate. For this traction, the S0-mode is excited, so the group velocity c_g^{ex} in Eq. (8) is S0-group velocity c_g^{S0} . Here, the S0-excitation is appropriate because the S0-mode leads to larger reflections for these kinds of cracks.

The center part of Fig. 3 contains the evaluation point P . The envelope of the y -displacement is evaluated as a time series. As described above, the y -component is of practical relevance as it can be measured using a single laser Doppler vibrometer. Figure 4 shows the y -displacement at point P in gray and the envelope as a black curve over the signal of different crack positions.

The right side of Fig. 3 shows the defect. All 1D finite elements and the scaling center in this part of the domain are dependent of the parameter vector \mathbf{q} . A double node is inserted into a super-element based on continued-fraction. The resulting inner traction-free boundary is marked in red with a white border in Fig. 3. Note that the continued-fraction approach handles the singular stress at the end of

this crack model. In total, the model has 180 (complex-valued) degrees of freedom. This low number is possible because the semi-analytical approach approximates the large undamaged part of the waveguide. At this center frequency, the wavelength is approximately 25 mm for the S0 mode and approximately 12 mm for the A0 mode. With other simulation methods, this leads to a much higher computational effort.

There are three parameters for the optimization. These parameters change the defect and its location. The first parameter q_1 defines the global position of the crack by shifting the super element Ω_5 along the x axis and changing the length of the super element Ω_4 accordingly. The second and third parameters control the crack length and angle by moving the crack tip inside the super element Ω_5 relative to the boundary. The maximal and minimal values for the parameters are listed in Table II. The crack length is between 0.25 and 2.6 mm. Here, the parameters are restricted to allow a numerically stable solution. Similar parameter restrictions can be found in other publications like Ref. 5.

The objective function value of the optimization problem (5) for varying values of q_1 and q_2 is displayed in Fig. 6(a). Here, q_3 is held constant at 1.5, i.e., only cracks orthogonal to the surface are considered. The artificial target measurement corresponds to the midpoint of the parameter space. The surface is relatively smooth and has only a few local minima. The global minimum at $(1.5, 1.5, 1.5)^T$ clearly has the lowest value. Using the result of Algorithm 1 as refined initial guess, the defect properties can be obtained by applying the IRGN method Algorithm 2 without any need for using a more in-depth initial guess search.

Another important aspect of an inverse method, especially in view of the measurement data, is its performance under noise. To analyze the performance of the proposed optimization algorithm, we create artificial measurement data by a single forward simulation with a parameter vector \mathbf{q}^* and add random noise to this target signal. The noise is defined in terms of the excitation pulse. The same threshold as for the time of flight is used to identify the excitation pulse. In Fig. 4(a), the dashed line shows this threshold. The excitation pulse is to the left of the dashed line. A noise level of 10^{-2} and 10^{-3} means that a normal-distributed noise with vanishing mean value and a standard deviation of 1% and 0.1% of the maximum amplitude of the excitation pulse has been added to the target signal, respectively. The envelope of the target signal is calculated afterward. Figure 6(b) shows the reconstruction error $|q_i^{\text{min}} - q_i^*|$ per parameter for the midpoint of the parameter space. Here, the first parameter, the global position of the crack, shows the

TABLE II. Parameters for the waveguide with a crack, where the origin of q_2 and q_3 is the center of Ω_5 .

Description	Parameter	Min	Max	Unit
Global x -position of Ω_5	q_1	200	2200	mm
Local x -position of the crack tip inside Ω_5	q_2	-0.5	+0.5	mm
Local y -position of the crack tip inside Ω_5	q_3	-2.25	0	mm

TABLE I. Material parameters for structural steel.

Isotropic material					
E :	200	GPa	ν :	0.3	
			ρ :	7.85	g cm^{-3}

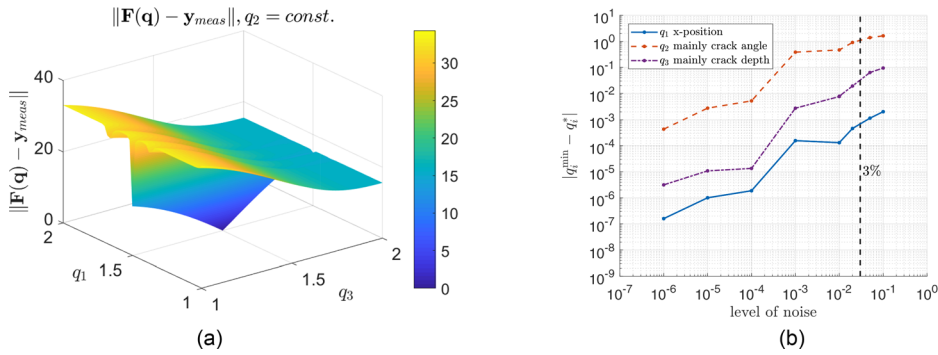


FIG. 6. (Color online) The objective function and reconstruction with noisy data for the waveguide with a crack, where the target parameter \mathbf{q}^* and the associated artificial measurement signal \mathbf{y}_{meas} correspond to the midpoint of the parameter space. (a) Objective function for varying parameters q_1 and q_3 . (b) Reconstruction error of parameters $|q_i^{min} - q_i^*|$ with noisy data.

smallest error. A lower error in the first parameter is also expected because the range in the physical space is much larger compared to the other parameters—see Table II. Translating the error in the physical space, the error stays under 1 mm for a noise level under 3%, which is a satisfactory level of precision for most applications. The error in the second parameter, on the other hand, shows lower robustness to noise. This parameter, which is linked to the crack angle, is likely to produce incorrect results. However, the more critical third parameter, which is more related to the crack length, has a significantly lower reconstruction error. In general, this investigation is only valid for the current target parameter \mathbf{q}^* ; as the crack length gets smaller with the third parameter, it is also expected that the error increases due to the negative influence of the noise. In conclusion, there are also physical boundaries to an appropriate parameter space depending on the noise inside the experimental data.

Figure 7(a) shows the convergence of the reconstruction error with a noise level of 10^{-5} . This noise level is introduced to prevent an “Inverse Crime” as both the target data and the reconstruction algorithm use the same simulation method. We observe an asymptotic rate of decline that, as theoretically expected, coincides with the rate of the regularization parameter in Algorithm 2.

To further validate the inverse method, ten different target parameters are randomly drawn. Noise with a standard deviation of 10^{-5} is added to the corresponding signals, and the parameters are reconstructed. Table III lists the reconstruction error for these points. For all reconstructions, the error is below 1%.

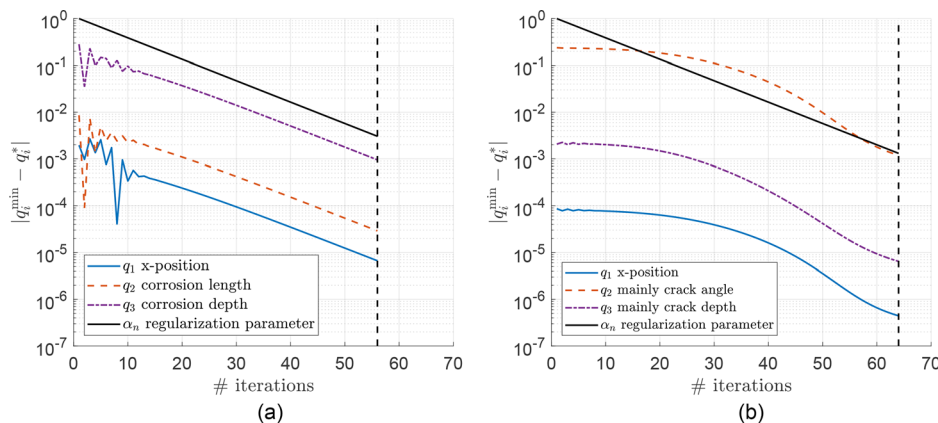


FIG. 7. (Color online) Error in the reconstruction procedure with a small amount of additional noise of 10^{-5} , where the target parameter \mathbf{q}^* is the center of the parameter space. (a) Error in the reconstruction for the waveguide with a crack. (b) Error in the reconstruction for the waveguide with a corrosion defect.

B. Waveguide with a delamination

This example considers a plate with a single straight horizontal delamination model. Figure 8 shows an overview of the model. Note that once again, the x axis is interrupted at some places to fit the model into the figure. The two colors inside the figure indicate that these defects are often present between two different layers. However, the material of these layers in our example is the same steel.

Prior investigations have shown that the A0-excitation will lead to larger reflections for delaminations. The traction is chosen accordingly as

$$f_{A0}(\mathbf{x}) = (0, -1)^T [\mathbf{x} \in \Gamma_\tau]. \tag{13}$$

Hence, c_g^{ex} in Eq. (8) is the A0-group velocity c_g^{A0} at the center frequency—see Fig. 2(b). The center of Fig. 8 highlights again the evaluation point P , where the envelope of the y -component of the displacement is taken as the data. The right part of Fig. 8 contains the defect. Here, the 1D finite elements and the scaling centers are affected by the parameters q_i . The delamination is modeled by inserting double nodes in two super elements. The SBFEM semi-analytical solution again captures the points with singular stresses.

There are two parameters for the optimization. The first parameter q_1 denotes the global position of the delamination. The second parameter changes the length of the delamination. The maximal and minimal values for the parameters are listed in Table IV.

Figure 9(a) depicts the objective function dependent on q_1 and q_2 . As in the previous example, the target signal is

TABLE III. Error for reconstruction \mathbf{q}^{\min} for differently shaped defects $\mathbf{q}^* \in [1, 2]^3$ for the waveguide with a crack with a noise level of 10^{-5} .

q_1^*	1.33	1.73	1.72	1.58	1.58	1.43	1.46	1.54	1.71	1.31
q_2^*	1.25	1.54	1.57	1.37	1.50	1.52	1.34	1.42	1.40	1.37
q_3^*	1.47	1.67	1.74	1.69	1.68	1.38	1.41	1.40	1.47	1.46
$\ \mathbf{q}^{\min} - \mathbf{q}^*\ $	2E-5	3E-3	2E-3	6E-4	5E-3	7E-4	1E-4	1E-4	4E-4	5E-6

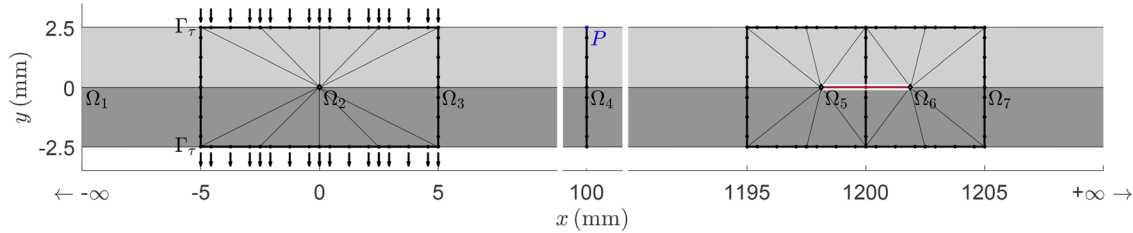


FIG. 8. (Color online) SBFEM-model for the waveguide with a delamination with degree $p = 4$. The defect is marked in red with a white border around $x = 1200$ mm.

TABLE IV. Parameters for the waveguide with a delamination.

Description	Parameter	Min	Max	Unit
Global x -position of Ω_5, Ω_6	q_1	200	2200	mm
Delamination length inside Ω_5, Ω_6	q_2	2.5	7.5	mm

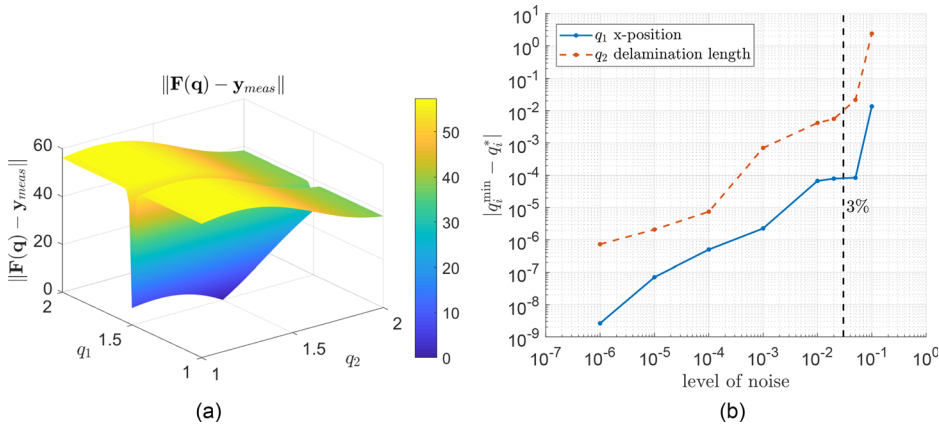


FIG. 9. (Color online) The objective function and reconstruction with noisy data for the waveguide with a delamination, where the target parameter \mathbf{q}^* and the associated artificial measurement signal \mathbf{y}_{meas} correspond to the midpoint of the parameter space. (a) Objective function for varying parameters q_1 and q_2 . (b) Reconstruction error of parameters $|q_i^{\min} - q_i^*|$ with noisy data.

TABLE V. Error for reconstruction \mathbf{q}^{\min} for differently shaped defects $\mathbf{q}^* \in [1, 2]^2$ for the waveguide with a delamination with a noise level of 10^{-5} .

q_1^*	1.45	1.28	1.29	1.35	1.66	1.54	1.33	1.47	1.26	1.69
q_2^*	1.69	1.38	1.27	1.59	1.67	1.39	1.44	1.43	1.29	1.32
$\ \mathbf{q}^{\min} - \mathbf{q}^*\ $	1E-6	1E-5	7E-6	2E-7	2E-6	8E-6	4E-6	3E-6	1E-5	9E-6

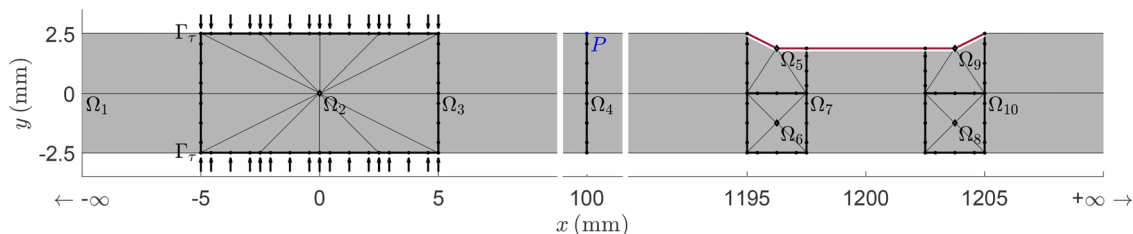


FIG. 10. (Color online) SBFEM-model for the waveguide with a corrosion defect with degree $p = 4$. The \mathbf{q} -dependent defect is marked in red with a white border around $x = 1200$ mm.

TABLE VI. Parameters for the waveguide with a corrosion defect.

Description	Parameter	Min	Max	Unit
Global x -position of $\Omega_5, \dots, \Omega_9$	q_1	200	2200	mm
Corrosion length on the surface	q_2	7.5	57.5	mm
Corrosion depth	q_3	0.25	1.00	mm

generated with the midpoint of the parameter space for \mathbf{q}^* . Figures 9(a) and 6(a) show a similar shape, but the two side channels with local minima are not present in this example. These side channels are missing because delaminations in the center of a waveguide do not lead to mode conversion for the A0-mode.

For this example, we could set the regularization parameter $\alpha_n = 0$ and achieve convergence within five iteration steps. In Fig. 9(b), the error for reconstruction with noise is given. Both parameters show high robustness against the noise. Additionally, Table V lists the reconstruction error for ten different randomly drawn target parameters with a noise level of 10^{-5} . The error indicates a high level of precision.

In total, the model has 226 degrees of freedom. A single forward calculation is performed in under 4 s on a modern desktop computer, while the reconstruction is computed in less than 5 min, including all preprocessing steps. The time is averaged over 100 reconstructions.

C. Waveguide with a corrosion defect

The last example considers a steel plate with a simple model for a corrosion damage. The assumption is that parts of the steel are missing, and a tapering has formed in the waveguide as illustrated by Fig. 10. Note that again the x axis is interrupted. The traction f_{S0} is the same as in first example [Eq. (12)], which leads to an S0-mode excitation. The S0-mode shows greater sensitivity than the A0-mode to changes in thickness. Therefore, the S0-excitation is used. The two re-entrant corners³⁴ in sub-domains Ω_5 and Ω_9 are located at the scaling center to handle the possible singular stresses for a deep corrosion. The model has 210 degrees of freedom in total.

There are three parameters to be optimized. Once more, the first parameter defines the global position of the defect.

The second parameter defines the length of the corrosion by changing the size of the super element Ω_7 . The third parameter denotes the depth of the corrosion—see Fig. 10. The maximal and minimal values for the parameters are listed in Table VI. Figure 11(a) shows the objective function for a constant corrosion depth. The surface is more complicated due to the two main reflection points at the scaling centers, leading to mode conversion. As mentioned earlier, we had to increase the number of random vectors drawn for the initial guess because of the more complicated shape of the objective function. In Fig. 11(b) the error for reconstruction with noise is given. Additionally, Fig. 7(b) shows the convergence behavior for the reconstruction error at the midpoint of the parameter space. Despite the more complicated behavior of the objective function, the parameters show robustness against noise. For all ten tests, the reconstruction leads to small errors as listed in Table VII.

V. CONCLUSION

In the paper, we showed that a semi-analytical waveguide model given by SBFEM can be combined successfully with derivative-based optimization to reconstruct defects of different nature in a two-dimensional waveguide, even in the presence of noise. For this purpose, SBFEM is implemented in MATLAB, coupled with the AD tool ADiMat and embedded in an iterative solution procedure. The reconstruction can be performed on a standard desktop computer within a very moderate time such that our approach offers considerable runtime advantages compared to alternative methods. Three numerical tests were conducted to illustrate our approach: The first example covers a crack identification, the second one a delamination, and the third one a corrosion. In all three cases, the waveguides were made out of steel. In the cross-sectional models, the reconstruction with a minimal amount of data are possible. Only the envelope of the y -displacement at a single point is sufficient if a certain geometry of a single defect is assumed. Due to the limited number of local minima, the envelope curve shows the most promising features for an optimization. In all tests carried out, the approach demonstrates robustness against noise and varying defect parameters.

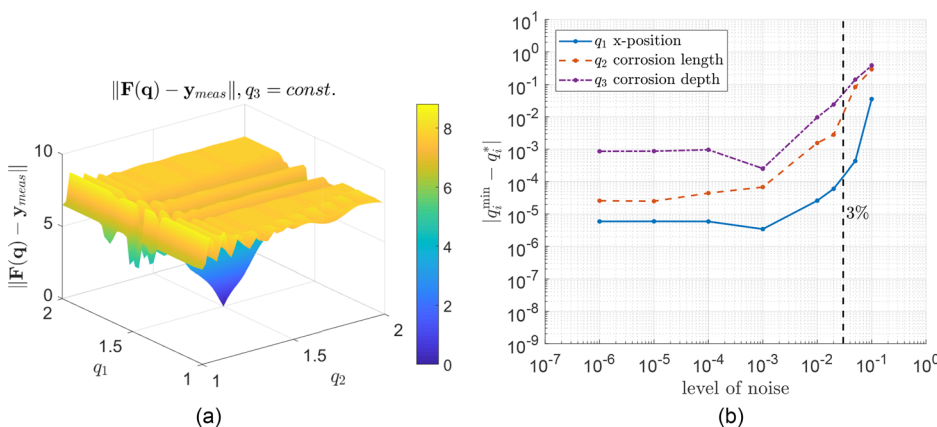


FIG. 11. (Color online) The objective function and reconstruction with noisy data for the waveguide with a corrosion defect, where the target parameter \mathbf{q}^* and the associated artificial measurement signal \mathbf{y}_{meas} correspond to the midpoint of the parameter space. (a) Objective function for varying parameters q_1 and q_2 . (b) Reconstruction error of parameters $|q_i^{min} - q_i^*|$ with noisy data.

TABLE VII. Error for reconstruction \mathbf{q}^{\min} for differently shaped defects $\mathbf{q}^* \in [1, 2]^3$ for the waveguide with a corrosion defect with a noise level of 10^{-5} .

q_1^*	1.59	1.51	1.47	1.35	1.55	1.28	1.52	1.42	1.34	1.40
q_2^*	1.43	1.67	1.28	1.55	1.46	1.53	1.44	1.67	1.29	1.42
q_3^*	1.48	1.33	1.44	1.49	1.57	1.42	1.52	1.64	1.54	1.37
$\ \mathbf{q}^{\min} - \mathbf{q}^*\ $	9E-4	9E-4	9E-4	8E-4	9E-4	8E-4	9E-4	9E-4	9E-4	9E-4

Future work will be dedicated to the extension of the three-dimensional case and anisotropic material behavior. The future work will allow the use of the proposed approach for non-destructive testing and structural health monitoring in real-life applications like carbon-enforced structures.

ACKNOWLEDGMENTS

The authors gratefully acknowledge the German Research Foundation for funding (DFG Project No. 428590437).

APPENDIX: IMPLEMENTATION DETAILS

This appendix shows how the Lyapunov equation can be solved with the help of an eigenvalue decomposition. The Lyapunov equation is

$$\mathbf{A}\mathbf{X} + \mathbf{X}\mathbf{A}^H + \mathbf{B} = \mathbf{0}. \tag{A1}$$

Define the right eigenvalue decomposition of \mathbf{A}

$$\mathbf{V}^{-1}\mathbf{A}\mathbf{V} = \mathbf{D} \tag{A2}$$

with the right eigenvector matrix \mathbf{V} and the diagonal eigenvalue matrix \mathbf{D} . Note that this leads to the left eigenvalue decomposition of \mathbf{A}^H

$$\mathbf{V}^H\mathbf{A}^H\mathbf{V}^{-H} = \mathbf{D}^H. \tag{A3}$$

After pre-multiplying with \mathbf{V}^{-1} and post-multiplying with \mathbf{V}^{-H} , Eq. (A1) leads to a new Lyapunov equation with a diagonal coefficient matrix

$$\mathbf{D}\tilde{\mathbf{X}} + \tilde{\mathbf{X}}\mathbf{D}^H + \tilde{\mathbf{B}} = \mathbf{0} \tag{A4}$$

with

$$\tilde{\mathbf{B}} = \mathbf{V}^{-1}\mathbf{B}\mathbf{V}^{-H} \quad \text{and} \quad \tilde{\mathbf{X}} = \mathbf{V}^{-1}\mathbf{X}\mathbf{V}^{-H}. \tag{A5}$$

The matrix $\tilde{\mathbf{X}}$ can be computed element-wise by

$$(\tilde{\mathbf{X}})_{ij} = \frac{-(\tilde{\mathbf{B}})_{ij}}{(\mathbf{D})_{ii} + (\mathbf{D})_{jj}^H}. \tag{A6}$$

The solution matrix \mathbf{X} of the original Lyapunov equation can be derived by the inverse of Eq. (A5), i.e., $\mathbf{X} = \mathbf{V}^H\tilde{\mathbf{X}}\mathbf{V}$.

¹J.-B. Ihn and F.-K. Chang, "Pitch-catch active sensing methods in structural health monitoring for aircraft structures," *Struct. Health Monit.* **7**(1), 5–19 (2008).
²N. Mori, S. Biwa, and T. Kusaka, "Damage localization method for plates based on the time reversal of the mode-converted Lamb waves," *Ultrasonics* **91**, 19–29 (2019).

³X. Zhao, R. L. Royer, S. E. Owens, and J. L. Rose, "Ultrasonic Lamb wave tomography in structural health monitoring," *Smart Mater. Struct.* **20**(10), 105002 (2011).
⁴R. Neubeck, C. Kexel, and J. Moll, "Matrix techniques for Lamb-wave damage imaging in metal plates," *Smart Mater. Struct.* **29**(11), 117003 (2020).
⁵K. Agathos, E. Chatzi, and S. P. Bordas, "Multiple crack detection in 3D using a stable xfem and global optimization," *Comput. Mech.* **62**(4), 835–852 (2018).
⁶J. Jung and E. Taciroglu, "Modeling and identification of an arbitrarily shaped scatterer using dynamic XFEM with cubic splines," *Comput. Methods Appl. Mech. Eng.* **278**, 101–118 (2014).
⁷M. A. Livani, N. Khaji, and P. Zakian, "Identification of multiple flaws in 2D structures using dynamic extended spectral finite element method with a universally enhanced meta-heuristic optimizer," *Struct. Multidisc. Optim.* **57**(2), 605–623 (2018).
⁸D. Rabinovich, D. Givoli, and S. Vigdergauz, "XFEM-based crack detection scheme using a genetic algorithm," *Int. J. Numer. Methods Eng.* **71**(9), 1051–1080 (2007).
⁹D. Rabinovich, D. Givoli, and S. Vigdergauz, "Crack identification by 'arrival time' using XFEM and a genetic algorithm," *Int. J. Numer. Methods Eng.* **77**(3), 337–359 (2009).
¹⁰E. Amitt, D. Givoli, and E. Turkel, "Time reversal for crack identification," *Comput. Mech.* **54**(2), 443–459 (2014).
¹¹C. Lopatin, D. Rabinovich, D. Givoli, and E. Turkel, "Computational time reversal for NDT applications using experimental data," *J. Nondestruct. Eval.* **36**(3), 48 (2017).
¹²R. Seidl and E. Rank, "Iterative time reversal based flaw identification," *Comput. Math. Appl.* **72**(4), 879–892 (2016).
¹³P. Broumand, "Inverse problem techniques for multiple crack detection in 2D elastic continua based on extended finite element concepts," *Inv. Probl. Sci. Eng.* **29**, 1702–1727 (2021).
¹⁴J. Rao, M. Ratsassepp, and Z. Fan, "Guided wave tomography based on full waveform inversion," *IEEE Trans. Ultrason. Ferroelectr. Freq. Control* **63**(5), 737–745 (2016).
¹⁵J. Rao, M. Ratsassepp, and Z. Fan, "Investigation of the reconstruction accuracy of guided wave tomography using full waveform inversion," *J. Sound Vib.* **400**, 317–328 (2017).
¹⁶J. Rao, J. Yang, M. Ratsassepp, and Z. Fan, "Madis Ratsassepp, and Zheng Fan. Multi-parameter reconstruction of velocity and density using ultrasonic tomography based on full waveform inversion," *Ultrasonics* **101**, 106004 (2020).
¹⁷Z. P. Wu, G.-R. Liu, and X. Han, "An inverse procedure for crack detection in anisotropic laminated plates using elastic waves," *Eng. Comput.* **18**(2), 116–123 (2002).
¹⁸H. Gravenkamp, J. Prager, A. A. Saputra, and C. Song, "The simulation of Lamb waves in a cracked plate using the scaled boundary finite element method," *J. Acoust. Soc. Am.* **132**(3), 1358–1367 (2012).
¹⁹C. Song and J. P. Wolf, "The scaled boundary finite-element method—a primer: Solution procedures," *Comput. Struct.* **78**(1-3), 211–225 (2000).
²⁰J. P. Wolf and C. Song, "The scaled boundary finite-element method—a primer: Derivations," *Comput. Struct.* **78**(1-3), 191–210 (2000).
²¹H. Gravenkamp, C. Birk, and C. Song, "Simulation of elastic guided waves interacting with defects in arbitrarily long structures using the scaled boundary finite element method," *J. Comput. Phys.* **295**, 438–455 (2015).
²²H. Gravenkamp, C. Song, and J. Prager, "A numerical approach for the computation of dispersion relations for plate structures using the scaled boundary finite element method," *J. Sound Vib.* **331**(11), 2543–2557 (2012).
²³H. Gravenkamp, C. Birk, and C. Song, "Computation of dispersion curves for embedded waveguides using a dashpot boundary condition," *J. Acoust. Soc. Am.* **135**(3), 1127–1138 (2014).

- ²⁴F. Krome and H. Gravenkamp, "A semi-analytical curved element for linear elasticity based on the scaled boundary finite element method," *Int. J. Numer. Methods Eng.* **109**(6), 790–808 (2017).
- ²⁵F. Krome, H. Gravenkamp, and C. Birk, "Prismatic semi-analytical elements for the simulation of linear elastic problems in structures with piecewise uniform cross section," *Comput. Struct.* **192**, 83–95 (2017).
- ²⁶P. Wasmer, F. Krome, J. Bulling, and J. Prager, "A fluid model for the simulation of fluid-structure interaction in the scaled boundary finite element method for prismatic structures," *PAMM* **18**(1), e201800139 (2018).
- ²⁷C. Song, E. T. Ooi, and S. Natarajan, "A review of the scaled boundary finite element method for two-dimensional linear elastic fracture mechanics," *Eng. Fracture Mech.* **187**, 45–73 (2018).
- ²⁸T. Khajah, L. Liu, C. Song, and H. Gravenkamp, "Shape optimization of acoustic devices using the scaled boundary finite element method," *Wave Motion* **104**, 102732 (2021).
- ²⁹A. Griewank and A. Walther, *Evaluating Derivatives: Principles and Techniques of Algorithmic Differentiation* (SIAM, Philadelphia, 2008).
- ³⁰U. Naumann, "The art of differentiating computer programs," in *An Introduction to Algorithmic Differentiation* (SIAM, Philadelphia, 2011).
- ³¹E. Kausel, *Advanced Structural Dynamics* (Cambridge University Press, Cambridge, 2017).
- ³²H. Gravenkamp, "Efficient simulation of elastic guided waves interacting with notches, adhesive joints, delaminations and inclined edges in plate structures," *Ultrasonics* **82**, 101–113 (2018).
- ³³N. van der Aa, H. Ter Morsche, and R. Mattheij, "Computation of eigenvalue and eigenvector derivatives for a general complex-valued eigensystem," *Electron. J. Lin. Algebra* **16**, 300–314 (2007).
- ³⁴J. Bulling and H. Gravenkamp, "Comparison of different models for stress singularities in higher order finite element methods for elastic waves," *PAMM* **19**(1), e201900095 (2019).
- ³⁵J. Bulling, H. Gravenkamp, and C. Birk, "A high-order finite element technique with automatic treatment of stress singularities by semi-analytical enrichment," *Comput. Methods Appl. Mech. Eng.* **355**, 135–156 (2019).
- ³⁶K. Tschöke and H. Gravenkamp, "On the numerical convergence and performance of different spatial discretization techniques for transient elastodynamic wave propagation problems," *Wave Motion* **82**, 62–85 (2018).
- ³⁷D. Chen, C. Birk, C. Song, and C. Du, "A high-order approach for modeling transient wave propagation problems using the scaled boundary finite element method," *Int. J. Numer. Methods Eng.* **97**(13), 937–959 (2014).
- ³⁸M. H. Bazyar and C. Song, "A continued-fraction-based high-order transmitting boundary for wave propagation in unbounded domains of arbitrary geometry," *Int. J. Numer. Methods Eng.* **74**(2), 209–237 (2008).
- ³⁹C. Song and J. P. Wolf, "The scaled boundary finite-element method—alias consistent infinitesimal finite-element cell method—for elastodynamics," *Comput. Meth. Appl. Mech. Eng.* **147**(3-4), 329–355 (1997).
- ⁴⁰W. Xing, C. Song, and F. Tin-Loi, "A scaled boundary finite element based node-to-node scheme for 2D frictional contact problems," *Comput. Methods Appl. Mech. Eng.* **333**, 114–146 (2018).
- ⁴¹www.autodiff.org (Last viewed July 29, 2022).
- ⁴²C. H. Bischof, H. M. Bucker, B. Lang, A. Rasch, and A. Vehreschild, "Combining source transformation and operator overloading techniques to compute derivatives for MATLAB programs," in *Proceedings of the Second IEEE International Workshop on Source Code Analysis and Manipulation*, IEEE (2002), pp. 65–72.
- ⁴³A. Wächter and L. T. Biegler, "On the implementation of an interior-point filter line-search algorithm for large-scale nonlinear programming," *Math. Program.* **106**(1), 25–57 (2006).
- ⁴⁴C. Büskens and D. Wassel, "The esa nlp solver worhp," in *Modeling and Optimization in Space Engineering* (Springer, Berlin, 2012), pages 85–110.
- ⁴⁵B. Kaltenbacher, A. Neubauer, and O. Scherzer, *Iterative Regularization Methods for Nonlinear Ill-Posed Problems* (de Gruyter, Berlin, 2008).
- ⁴⁶H. Gravenkamp, C. Song, and J. Zhang, "On mass lumping and explicit dynamics in the scaled boundary finite element method," *Comput. Methods Appl. Mech. Eng.* **370**, 113274 (2020).
- ⁴⁷Z. Su and L. Ye, "Selective generation of lamb wave modes and their propagation characteristics in defective composite laminates," *Proc. Inst. Mech. Eng., Part L: J. Mater.: Des. Appl.* **218**(2), 95–110 (2004).